Atmospheric Environment 214 (2019) 116850

Contents lists available at ScienceDirect

Atmospheric Environment

journal homepage: www.elsevier.com/locate/atmosenv

Impact of planetary boundary layer structure on the formation and evolution of air-pollution episodes in Shenyang, Northeast China

Xiaolan Li[a,*], Xiao-Ming Hu[b], Yanjun Ma[a,**], Yangfeng Wang[a], Liguang Li[a], Ziqi Zhao[a]

[a] Institute of Atmospheric Environment, China Meteorological Administration, Shenyang, Liaoning, 110166, China
[b] Center for Analysis and Prediction of Storms, and School of Meteorology, University of Oklahoma, Norman, OK, 73072, USA

ARTICLE INFO

Keywords:
Air pollution
Planetary boundary layer structure
Low-level jet
Convective turbulence
Tracer simulation

ABSTRACT

The impact of the planetary boundary layer (PBL) structure on air pollution in Northeast China, where frequently experiences air pollution episodes in autumn and winter, is not well understood due to a lack of observations. In this study, four pollution episodes during autumn and winter of 2016 at Shenyang, a provincial capital city in Northeast China, were examined to investigate the linkage between the PBL structure and air pollution using meteorological sounding data and LiDAR-retrieved profiles of aerosol extinction coefficients. We also conducted a tracer simulation using the Weather Research and Forecasting model with Chemistry (WRF-Chem) to demonstrate the transport and vertical mixing of air pollutants in the PBL. The results indicated that a stable, moist and shallow surface layer (< 400 m) formed and remained at night due to strong surface radiative cooling after a steep decline of temperature during the first air-pollution episode (EP1, from 12:00 Local Time (LT) on November 26 to 07:00 LT on November 27). Stable stratification and stagnant winds contributed to the increase of surface pollutant concentrations in EP1. Strong surface potential temperature inversion and enhanced local emissions during evening rush hour resulted in the formation of EP2 (13:00–23:00 LT on December 2). Observations and modelling results revealed that large amount of pollutants were transported by the southerly nocturnal low-level jets from the North China Plain to Shenyang after EP2. These pollutants were trapped in the residue layer at night and then mixed to the surface after sunrise due to convective turbulence, leading to the formation of EP3 (06:00–23:00 LT on December 3). EP4 (03:00–14:00 LT on December 4) occurred in the convergence zone ahead of an approaching trough. Low wind speed (< 6 m s^{-1}) and high relative humidity (> 80%) in the PBL enhanced the deterioration of air quality near the surface.

1. Introduction

Air pollution can have adverse impacts on human and ecological health (Kampa and Castanas, 2008; Richardson et al., 2013; Avnery et al., 2011), cause low visibility and traffic safety issues (Chen et al., 2012; Armah et al., 2010), and affect weather and climate change (Kan et al., 2012; Ding et al., 2013; Seinfeld and Pandis, 2016). The frequent occurrence of heavy air pollution events in China is an urgent environmental problem (Chen et al., 2013; Guo et al., 2014; Ye et al., 2016).

To understand the potential causes of air pollution in China, the physical, chemical, and optical properties of aerosol particles and the meteorological conditions during severe pollution episodes have been widely investigated in different heavily polluted regions, including the North China Plain (Zhao et al., 2013; Ye et al., 2016; Han et al., 2018), central and eastern China (Zhao et al., 2009; Wang et al., 2014; Zhang et a., 2014; Che et al., 2018), the Pearl River Delta (Ansmann et al., 2005; Wu et al., 2007; Zhang et al., 2013), the Yangtze River Delta (Cheng et al., 2014; Wang et al., 2015), the Sichuan Basin (Tao et al., 2014; Wang et al., 2017), and the Northeast China (Li et al., 2018a, 2018b; Ma et al., 2018; Zhao et al., 2018a, 2018b). These studies have revealed that air pollution depends primarily on local emissions, photochemical reactions, and meteorological features (Chen et al., 2008; Liu et al., 2009; Zhu et al., 2012; Hu et al., 2014, 2016), including the thermodynamic and dynamic structures of the planetary boundary layer (PBL) (Bressi et al., 2013; Gao et al., 2016; Tang et al., 2016; Wei et al., 2018).

The thermodynamic structure of the PBL determines the vertical mixing of air pollutants. Within a convective boundary layer, air pollutants tend to mix uniformly due to convective turbulence and eddies

* Corresponding author.
** Corresponding author.
E-mail address: leexl.ouc@163.com (X. Li).

https://doi.org/10.1016/j.atmosenv.2019.116850
Received 22 May 2019; Received in revised form 17 July 2019; Accepted 19 July 2019
Available online 22 July 2019
1352-2310/

of different sizes (Stull, 1988). In a stable boundary layer, with the presence of potential temperature inversions, vertical mixing is weak, which usually leads to the accumulation of local air pollutants (Li et al., 2018a; Miao and Liu, 2019). Such regular diurnal evolution of the PBL thermodynamic structure can affect surface concentrations of air pollutants (e.g., O_3) in the morning and at subsequent peaks during the day, as revealed by previous observations and numerical simulations (Athanassiadis et al., 2002; Hu et al., 2013a, 2013b, 2018).

The dynamic structure of the PBL, including wind shears and turbulence, can modify air quality by influencing the dispersion/transport processes of air pollutants. For example, the impacts on air pollution by low-level jets (LLJs) characterized by strong vertical wind shears in the PBL and turbulence has been investigated in different regions worldwide. Klein et al. (2014) analyzed the role of nocturnal LLJs in modifying urban O_3 concentrations and air quality during summer over the southern Great Plains of United States. Wei et al. (2018) observed that intermittent turbulence triggered by LLJs resulted in dispersion of air pollutants and improved air quality in the North China Plain. Hu et al. (2013b) indicated that LLJs probably impacted air quality in Oklahoma City, United States by modifying the nocturnal urban heat island. Ren et al. (2019) analyzed the effects of turbulence structures on heavy haze pollution episodes in urban and suburban areas in Beijing. However, due to the lack of high vertical-resolution observations of meteorological parameters and air pollutants, the impact of PBL structure on air pollution remains unclear in some regions in China.

In recent years, progressively more comprehensive observational campaigns related to the PBL have been carried out in different heavily polluted regions of China. Han et al. (2018) analyzed the effect of PBL structure on the rapid formation and evolution of a typical haze-fog event in Tianjin, a megacity in the North China Plain, using vertical profiles of fine particulate matter ($PM_{2.5}$) concentrations and meteorological parameters. Liu et al. (2015) observed that weak winds, low PBL height, and a thermal inversion layer greatly contributed to the formation of a typical haze event in January of 2014 in the Pearl River Delta region. Zhong et al. (2018) evaluated the relative contributions of PBL meteorological factors to the explosive growth of $PM_{2.5}$ during 12 persistent heavy aerosol pollution episodes in Beijing. However, similar observational campaigns have rarely been conducted in Northeast China (Li et al., 2018a; Ma et al., 2018), despite the frequent occurrence of severe air pollution episodes in this region.

Shenyang, a provincial capital city in the Northeast China, experiences serious air pollution, especially in autumn and winter. Therefore, a PBL observational campaign was held in this city from November 19 to December 6, 2016, and the influencing role of PBL vertical structures on air pollution was examined during four air pollution episodes. High-resolution profiles of meteorological parameters and aerosol extinction coefficients were obtained from sounding systems and a ground-based LiDAR. We also conducted a three-dimensional (3D) tracer simulation using the Weather Research and Forecasting model with Chemistry (WRF-Chem) to analyze the transport and vertical distribution of air pollutants.

The rest of this paper is organized as follows. Section 2 introduces the study area, observational data, and setup of the tracer simulations with WRF-Chem in detail. Section 3 analyzes the characteristics of PBL structure and their effect on the formation and evolution of four air pollution episodes. Conclusions are drawn in Section 4.

2. Data and method

2.1. Study area, observational sites and data

Shenyang, located in the southern region of Northeast China (Fig. 1), is the capital of Liaoning Province. Its population reached 7.35 million in 2017 (http://www.ln.stats.gov.cn/tjsj/sjcx/ndsj/otherpages/2018/indexch.htm). Air pollution in Shenyang is greatly affected by local anthropogenic emissions (Ma et al., 2018), and is commonly

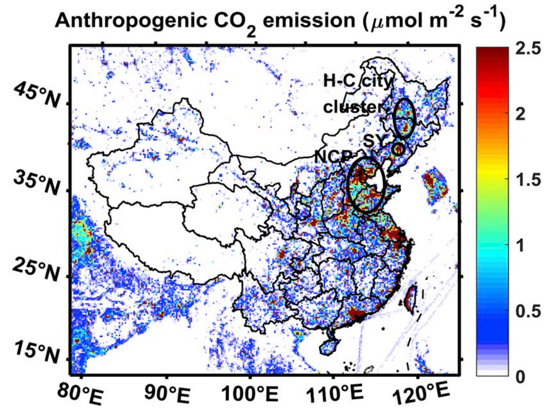

Fig. 1. Domain configuration for tracer simulations using WRF-Chem, with the background shading showing the spatial distributions of 0.5° × 0.5° ODIAC anthropogenic CO_2 emissions in 2016. Black circles marked the locations of Shenyang (short for SY), the North China Plain (NCP), and Harbin–Changchun (H–C) city cluster.

exacerbated by the long-range transport of air pollutants from the North China Plain (Li et al., 2018a; Miao et al., 2018) and/or from the Harbin–Changchun city cluster (Li et al., 2018b). Fig. 1 shows the spatial distribution of anthropogenic CO_2 emissions over China in 2016, which was obtained from the 2016 version of the Open-source Data Inventory for Anthropogenic CO_2 (ODIAC) emission dataset (Oda et al., 2018). Even though CO_2 is not a direct precursor of haze pollution, its emission has a high correlation with the emissions of haze precursors such as $PM_{2.5}$, NO_x, and SO_2, particularly in urban cities (Lin et al., 2018). Therefore, the CO_2 was used here as a surrogate of the general emission of air pollutants.

Three observational stations, with a distance between each two stations less than 8 km, are located in the southern urban region of Shenyang (Fig. 2a). The accuracy of observational variables and information about the devices at the three stations are summarized in Table 1. A PBL observational campaign was conducted at the balloon sounding station (41.6841°N, 123.4160°E) from November 19 to December 6, 2016, to measure high-resolution vertical profiles of wind speed (WS), wind direction (WD), air temperature (T_a), and relative humidity (RH). The balloons were released eight times each day, starting at 02:00 local time (LT) and with an interval of 3 h. We followed the method described in Li et al. (2018a) to execute data quality control and then obtained 10-m vertical resolution profiles of these meteorological parameters as well as potential temperature (θ). Detailed information about the balloon sounding system can be found in Li et al. (2018a).

Vertical distributions of the aerosol extinction coefficient (σ_{ext}) were measured by a ground-based LiDAR that was installed at the top of an office building (about 60 m high; 41.7388°N, 123.4256°E) of the Institute of Atmospheric Environment, China Meteorological Administration (CMA). The LiDAR detection had a temporal resolution of 5 min, a vertical resolution of 7.5 m, and a blind zone of 45 m above its installation altitude. This station also provided atmospheric visibility observed at 60 m (Vis_H) at intervals of 5 min.

Conventional surface meteorological data, including hourly mean WS, WD, T_a, and RH at a height of 2 m and atmospheric visibility at 2.8 m height (Vis_L), were obtained from a national weather station (41.7352°N, 123.5100°E) in Shenyang. The national weather station also carried out routine meteorological sounding detection at 08:00 and 20:00 LT every day using an operational L-band radiosonde system (Guo et al., 2016). These L-band sounding data could be used to validate the intensive sounding measurements at the balloon sounding station.

Moreover, hourly mean mass concentrations of six criteria air pollutants ($PM_{2.5}$, PM_{10}, SO_2, NO_2, O_3, and CO) and the air quality index

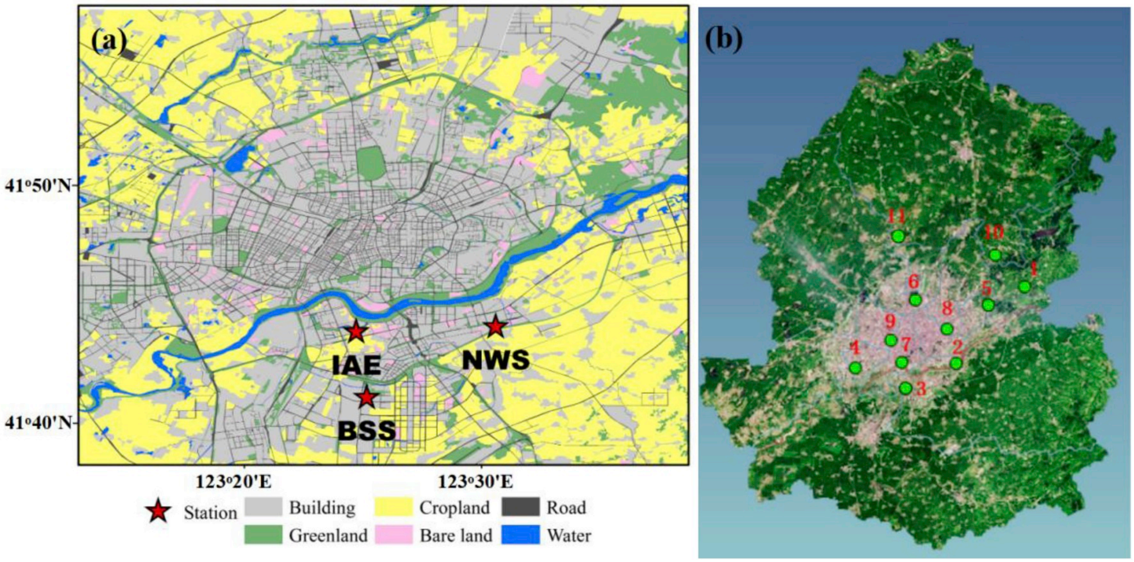

Fig. 2. (a) Land use types and (b) locations of 11 air quality monitoring stations in Shenyang. Red stars represent three observational stations. (For interpretation of the references to colour in this figure legend, the reader is referred to the Web version of this article.)

Table 1
Information of observational variables and devices at three stations in Shenyang.

Station	Variable	Interval	Height	Device	Accuracy
BSS	WS, WD, T_a, and RH	3 h	0–2 km at least	CZTK-1; IAP-CAS, China	WS: 0.1 m s^{-1}, WD: 0.1°, T_a: 0.1 °C, RH: 0.1%
NWS	Vis_L	1 h	2.8 m	DNQ1; Huayun, China	± 10%, 10 m–10 km ± 15%, 10–35 km
	WS, WD, T_a, RH, and Precipitation	1 h	2 m	ZQZ-CII Automatic weather station, Jiangsu Radio, China	WS: 0.1 m s^{-1}, WD: 0.1°, T_a: 0.1 °C, RH: 0.1%, Precipitation: 0.1 mm
	WS, WD, T_a, RH, and P_a	0800 and 2000 LT	0–2 km at least	GTS1 digital electronic radiosonde, Shanghai Changwang, China	T_a: 0.2 °C, 50 to −90 °C RH: 5%, $T_a \geq -25$ °C 10%, $T_a < -25$ °C P_a: 2 hPa, 1050–500 hPa 1 hPa, 500–5 hPa WS: 0.1 m s^{-1}; WD: 0.1°
IAE	Vis_H	10 min	60 m	FD12,Väsälä, Finland	± 10%, 10 m–10 km ± 20%, 10–50 km
	σ_{ext}	5 min	105 m–5 km	Lidar-D-2000; Wuxi CAS Photonics, China	< 30%, 0–0.1 km^{-1} < 10%, > 0.1 km^{-1}

(AQI) averaged at 11 monitoring stations in Shenyang (Fig. 2b) were obtained from the Liaoning real-time air quality publishing system (http://211.137.19.74:8089/) to analyze air quality during the study period. The detailed information of each station is available in Li et al. (2017). The hourly averaged air quality data at the 11 stations were used for further analysis.

2.2. Determination of the PBL height

Surface air quality is closely related to the evolution of PBL height. Based on the sounding data, we used the 1.5-θ-increase-method (Nielsen-Gammon et al., 2008) to determine the PBL height at daytime and the critical bulk Richardson number (R_i) method (Stull, 1988) to estimate the depth of a stable boundary layer at night. The two methods have been widely performed in many other PBL and pollution studies (Hu et al., 2014; Li et al., 2018a; Yang et al., 2019; Guo et al., 2016; Miao et al., 2017; Hong, 2010; Seidel et al., 2012). The 1.5-θ-increase-method defines the PBL height as the height where the θ first exceeds the minimum θ value within the boundary layer by 1.5 K, while the critical bulk Richardson number method defines the PBL height as the lowest height with R_i larger than 0.25. R_i represents the ratio of turbulence associated with buoyancy to that induced by mechanical shear. It can be calculated using profiles of potential temperature and wind speed, following the method in Guo et al. (2016).

2.3. Tracer simulation with WRF-Chem

CO_2 can be used as a tracer gas to study the transport of air pollutants in the atmosphere (Boering et al., 1996; Hintsa et al., 1998; Li et al., 2014). A 3D tracer simulation with WRF-Chem (version 3.9.1.1) was conducted to demonstrate the transport and mixing processes of CO_2 in the PBL based on the ODIAC emission dataset.

The simulation domain covered China (Fig. 1) and had a horizontal grid spacing of 20 km with 47 vertical layers[1] extending from the surface to 10 hPa. The initial and boundary conditions of meteorological variables and CO_2 were obtained from the National Centers for Environmental Prediction (NCEP)/DOE R2 data (Kanamitsu et al., 2002) and the output of the global model CarbonTracker with a resolution of 3° × 2° (Peters et al., 2007), respectively. The tracer simulation was initialized at 0000 UT (Universal Time) on January 1, 2016, and run

[1] The lowest 15 layers correspond to the heights of 12, 37, 62, 86, 111, 144, 186, 227, 290, 375, 460, 546, 634, 722, 834 m, respectively.

Table 2
Overview of parameterization schemes and nudging configurations for the WRF-VPRM simulations.

Parameterized process/Nudging configuration	Chosen scheme/configuration	Reference
Short wave radiation	Dudhia algorithm	Dudhia (1989)
Long wave radiation	Rapid radiative transfer model (RRTM)	Mlawer et al. (1997)
Boundary layer	Yonsei University (YSU) scheme	Hong et al. (2006)
Microphysics	Morrison microphysics scheme	Morrison et al. (2009)
Land surface model	Noah land-surface scheme	Chen and Dudhia (2001)
Cumulus	Grell-Freitas scheme	Wang and Kotamarthi (2014)
Interior nudging	Spectral nudging	
Nudging variables	Horizontal wind components, temperature, geopotential	
Nudging coefficient	$3 \times 10^{-5}\ s^{-1}$	
Nudging height	Above PBL	
Wave number	5 and 3 in the zonal and meridional directions respectively	
Nudging period	Throughout the downscaling simulation	

throughout the whole year using nudging and climate downscaling techniques. The nudging configuration and parameterization schemes selected for the simulation, which follow Hu et al. (2019), are summarized in Table 2.

3. Results

3.1. Variations of pollutant concentrations and meteorological parameters during four air pollution episodes

3.1.1. Identification and evolution of four air pollution episodes

An air pollution episode is defined here as a period between two adjacent lowest hourly mean AQI values with a highest hourly mean AQI larger than 150. According to this definition, four air pollution episodes were identified during the period of the PBL experiment in Shenyang; episode 1 (EP1) from 12:00 LT on November 26 to 07:00 LT on November 27, EP2 from 13:00 to 23:00 LT on December 2, the EP3 during 06:00–23:00 LT on December 3, and the EP4 during 03:00–14:00 LT on December 4.

The temporal variations of surface hourly mean AQI and mass concentrations of six criteria air pollutants during the four air pollution episodes are illustrated in Figs. 3a and 4a. During all episodes, except EP3, the hourly mean concentrations of all air pollutants, except O_3, increased substantially. The O_3 concentrations remained low mainly because of the titration effect of NO_x and the dry deposition of O_3 (Hu et al., 2012). However, during EP3, PM and O_3 concentrations increased, but the remaining pollutants remained unchanged (Fig. 4a). $PM_{2.5}$, the primary air pollutant during all four episodes according to the daily air quality records from the China National Environmental Monitoring Centre, reached a maximum concentration of 207, 135, 168, and 202 $\mu g\ m^{-3}$ during the four episodes, respectively.

To compare the characteristics of the four air pollution episodes further, Table 3 summarizes the duration and the mean values and standard deviations of the AQI and air pollutant concentrations for each episode. Overall, EP1 had the longest duration (20 h) and the highest AQI and concentrations of most air pollutants (except O_3 and NO_2). EP2 lasted for 11 h and was characterized by the lowest AQI and PM concentrations but the highest NO_2 and CO concentrations, which were partly related to enhanced local emissions during the evening rush hour on December 2, 2016. The highest O_3 and the lowest SO_2, NO_2, and CO

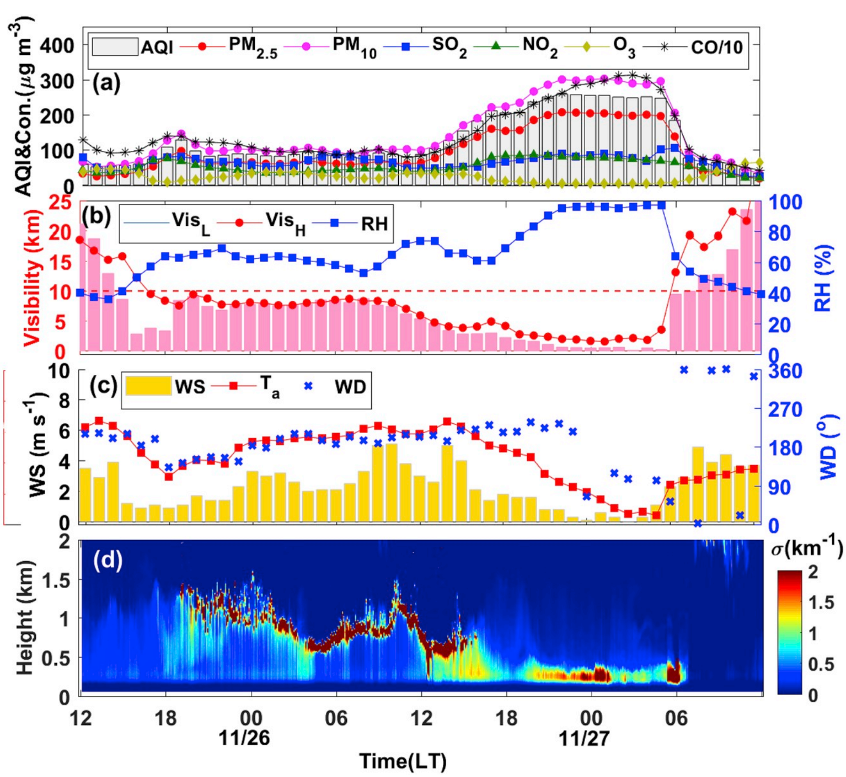

Fig. 3. Variations of hourly mean (a) air quality index and mass concentrations of $PM_{2.5}$, PM_{10}, SO_2, NO_2, O_3, and CO, (b) atmospheric visibility observed at 2.8 m (Vis_L) and 60 m (Vis_H) and relative humidity, (c) wind speed and direction and air temperature, and (d) vertical distribution of aerosol scattering coefficient within 2 km above the ground detected by a LiDAR in Shenyang from 12:00 LT on November 25 to 12:00 LT on November 27, 2016.

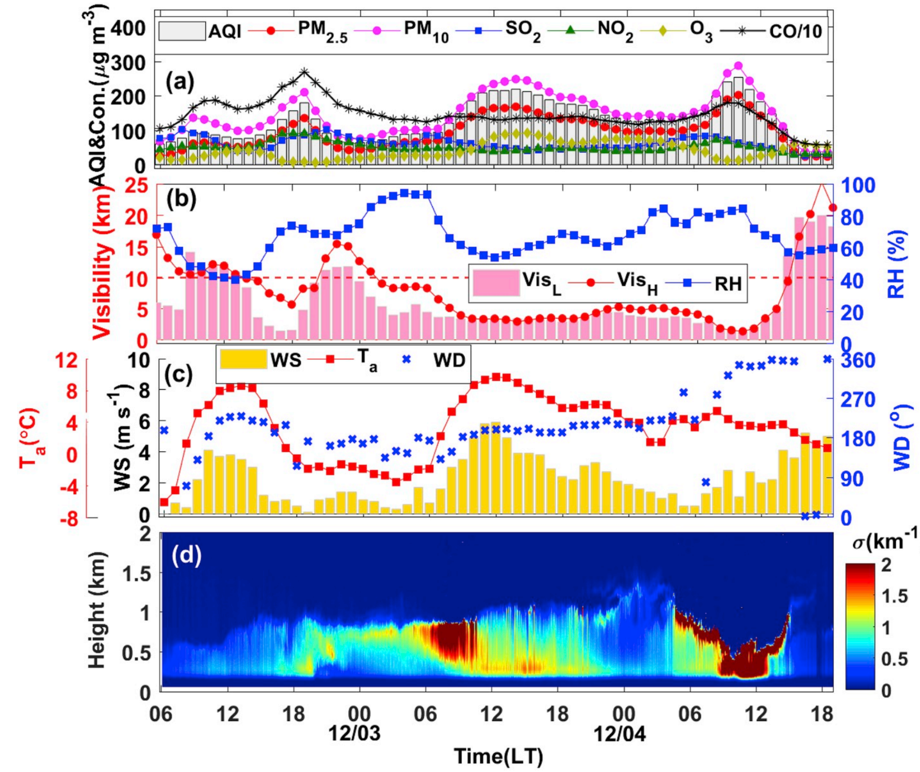

Fig. 4. Same as Fig. 3, but from 06:00 LT on December 2 to 18:00 LT on December 4, 2016.

Table 3
The duration and mean values and standard deviations of the AQI and six air pollutant concentrations during four air pollution episodes in 2016 in Shenyang. Bold font and underline represent the highest and lowest mean values, respectively.

Episode	Period	Duration	AQI	$PM_{2.5}$ μg m^{-3}	PM_{10} μg m^{-3}	SO_2 μg m^{-3}	NO_2 μg m^{-3}	O_3 μg m^{-3}	CO mg m^{-3}
EP1	1200 LT on Nov 26–0700 LT on Nov 27	20 h	**202 ± 61**	**158 ± 51**	**230 ± 74**	**74 ± 17**	69 ± 15	13 ± 11	**2.0 ± 0.8**
EP2	1300–2300 LT on Dec 2	11 h	105 ± 38	78 ± 31	130 ± 44	71 ± 23	**71 ± 15**	20 ± 15	**2.0 ± 0.4**
EP3	0600–2300 LT on Dec 3	18 h	167 ± 41	128 ± 32	188 ± 46	55 ± 13	44 ± 4	**63 ± 23**	1.3 ± 0.1
EP4	0300–1400 LT on Dec 4	12 h	168 ± 49	130 ± 41	183 ± 56	66 ± 15	53 ± 11	35 ± 19	1.4 ± 0.3

concentrations were observed during EP3. The pollution level of EP4 was generally close to that of EP3, but EP4 exhibited lower O_3 and higher SO_2 and NO_2 concentrations.

3.1.2. Variations of meteorological parameters during air pollution episodes

The temporal variations of meteorological parameters near the surface, including visibility, RH, T_a, WS, and WD during the four air pollution episodes are shown in Fig. 3b and c, as well as Fig. 4b and c. The two levels of visibility (Vis_L and Vis_H) showed similar trend, and both exhibited negative correlations with PM concentration and RH during all episodes, except for EP3 (Figs. 3b and 4b). Based on observations on hazy days in the North China Plain, Chen et al. (2012) found that low visibility at RH < 90% depended mainly on high aerosol volume concentrations, whereas a decrease in visibility at RH > 90% was influenced predominantly by an increase in RH. During EP1, extremely high RH (> 95%) largely contributed to extremely low visibility, about 77 and 156 m at 2.8 and 60 m heights, respectively (Fig. 3b). Such high RH during EP1 was partly related to a steep drop of T_a, from 4 °C to −8 °C during 14:00–22:00 LT on November 26 (Fig. 3c). Cold surface temperature usually leads to a stable and shallow surface layer due to strong radiative cooling during nighttime, which suppresses vertical dispersion of air pollutants. Additionally, stagnant winds favored the accumulation of air pollutants near the surface during EP1; the WS at 2 m height gradually approached zero from 14:00 LT on November 26 to 06:00 LT on November 27, corresponding to an average increase in surface $PM_{2.5}$ concentration of 12 μg m^{-3} h^{-1}. After this time, $PM_{2.5}$ concentration decreased rapidly with increasing WS (Fig. 3c).

Compared with EP1, the Vis_L and Vis_H values during EP2 was higher due lower PM concentrations and lower RH (40–75%) (Fig. 4b). Interestingly, the difference between Vis_L and Vis_H during EP2 was larger than that in other episodes, suggesting that air pollutants tended to concentrate at lower altitudes. This was partly related to enhanced local emissions near the surface during the evening rush hour. In addition, weak southerly flows (WS < 1 m s^{-1}) also contributed to the increase of PM concentration near the surface (Fig. 4c).

The relationships between pollutant concentrations and meteorological parameters during EP3 differed markedly from those in other episodes. $PM_{2.5}$ concentration exhibited a positive correlation with WS and a negative correlation with RH during EP3, which was likely related to the transport of air pollutants. Heavy air pollution was observed simultaneously in various cities in the North China Plain; the highest hourly mean $PM_{2.5}$ concentration reached nearly 500 μg m^{-3} in Beijing and Baoding and exceeded 600 μg m^{-3} in Shijiazhuang (Liu et al., 2019). Miao et al. (2017) reported that aerosols emitted from the North China Plain accounted for about 40% of the near-surface $PM_{2.5}$ concentration in Shenyang during this episode. Meanwhile, high daytime temperature on December 3 (9.6 °C at maximum, the highest record in December of 2016), which favored the formation of O_3 through photochemical reaction, was responsible for the high O_3 concentrations. During EP4, surface

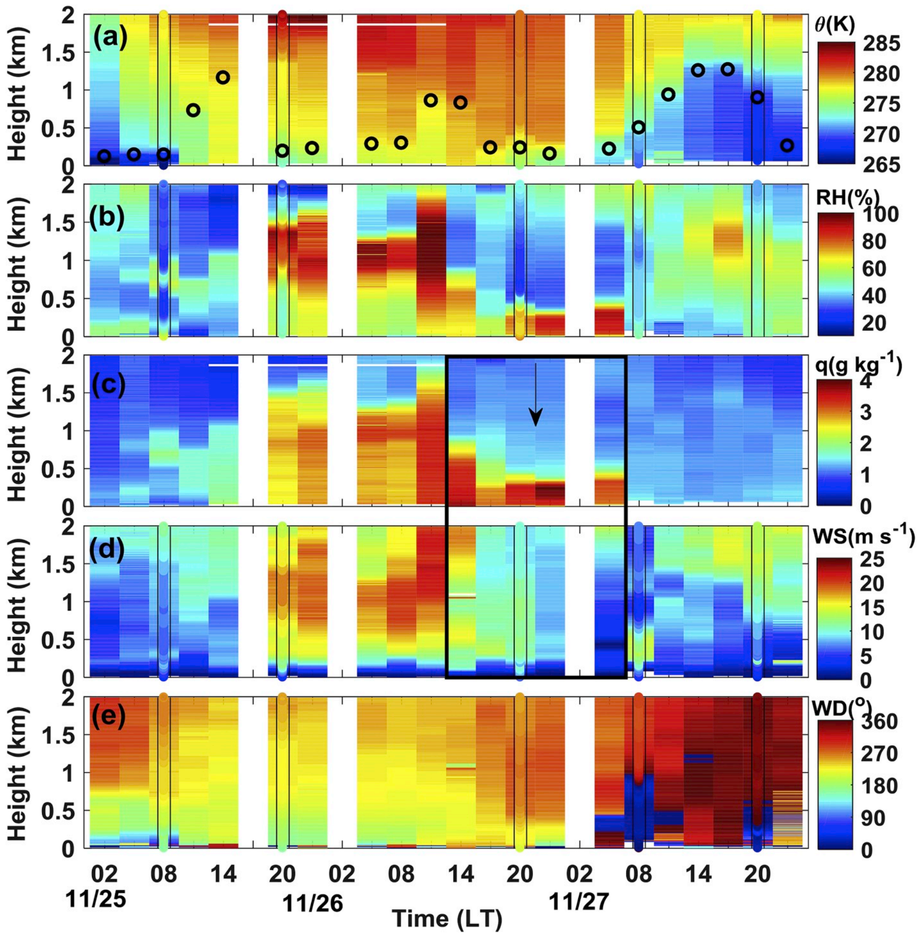

Fig. 5. Height-time variations of (a) potential temperature, (b) relative humidity, (c) specific humidity, (d) wind speed, and (e) wind direction below 2 km measured at the BSS in Shenyang on November 25–27, 2016. Color dots represent sounding profiles measured at the NWS at 08:00 and 20:00 LT, and black circles represent the PBL height. Four air pollution episodes are marked by rectangles with arrows representing the occurrence time of the highest AQI in each episode. (For interpretation of the references to colour in this figure legend, the reader is referred to the Web version of this article.)

PM concentration increased again, with a continuous decline of WS. The two levels of visibility were close to each other during EP3 and EP4, mainly due to vertical mixing of air pollutants during daytime.

In addition, southerly flows dominated during the development of all four air pollution episodes. Miao et al. (2018) reported that southerly winds were often observed during wintertime heavy pollution in Northeast China. Changes in WD corresponded with a decline of PM concentration in both EP1 and EP4. The WD eventually turned from south to north in both episodes.

3.1.3. Vertical distribution and evolution of aerosol extinction coefficient

The vertical distributions of the aerosol extinction coefficient (σ_{ext}) can reflect the vertical transport of air pollutants directly and the evolution of PBL structure indirectly. Therefore, examining σ_{ext} provides a better understanding of the formation and evolution of surface air pollution. Figs. 3d and 4d display the vertical distributions of σ_{ext} retrieved from the ground-based LiDAR during the four air pollution episodes.

In the early period of EP1 (12:00–17:00 LT on November 26), corresponding to the increase of surface PM concentration, the values of σ_{ext} below 800 m increased markedly and mostly ranged between 1.0 and 1.5 km^{-1}. After 20:00 LT on November 26, the depth of the aerosol-rich layer decreased to ~450 m, and the σ_{ext} values increased to more than 2.0 km^{-1}. Meanwhile, the surface PM concentration remained high (Fig. 3a). Trapping air pollutants in such a shallow layer contributed to the deterioration of air quality near the surface during EP1. In EP2, when the surface PM concentration reached peaks at around 20:00 LT on December 2, the largest σ_{ext} values (~1.3 km^{-1}) were observed beneath 400 m. Thereafter, the σ_{ext} below 300–500 m suddenly decreased, corresponding to a decline of surface PM concentration, while the σ_{ext} between 500 and 800 m increased markedly. Until the early morning of December 3, the maximum σ_{ext} was larger than 2.0 km^{-1} at the altitudes of 500–800 m. With the passage of time, this pollution layer gradually extended downward and ultimately reached the surface at about 10:00 LT. As a result, the surface PM concentration began to increase. During EP3, the σ_{ext} was about 1–1.5 km^{-1} at altitudes below 1 km, with the largest σ_{ext} observed below 400 m. After 18:00 LT on December 3, the σ_{ext} began to decrease at all altitudes, but it then suddenly increased after 04:00 LT on December 4, leading to the formation of EP4. During the development of EP4, all the σ_{ext} values below 600 m exceeded than 2.0 km^{-1}.

3.2. Characteristics of PBL structure and their impact on air pollution

3.2.1. Variations of PBL vertical structure

We examined the evolution of the vertical distributions of θ, RH, q, WS, and WD below 2 km as well as the PBL height during the four air pollution episodes (Figs. 5 and 6). The dots in Figs. 5 and 6 represent the measurements obtained from the L-band sounding system at the national weather station. Overall, the vertical distributions of the meteorological parameters measured at the balloon sounding station were basically consistent with those observed at the national weather station. This indicated the reliability of the sounding data during the PBL experiment. In addition, to display the PBL vertical structure clearly, Fig. 7 shows the composite profiles of θ, RH, and WS at 08:00 and 20:00 LT during these episodes measured at the national weather station.

During EP1, a stable surface layer with potential temperature inversions was observed at nighttime. The top of this layer was lower than 300 m. High RH (> 80%) and q (> 4 g kg^{-1}) and low WS were observed in this layer (Fig. 5a, b, 7a). The stable stratification, weak

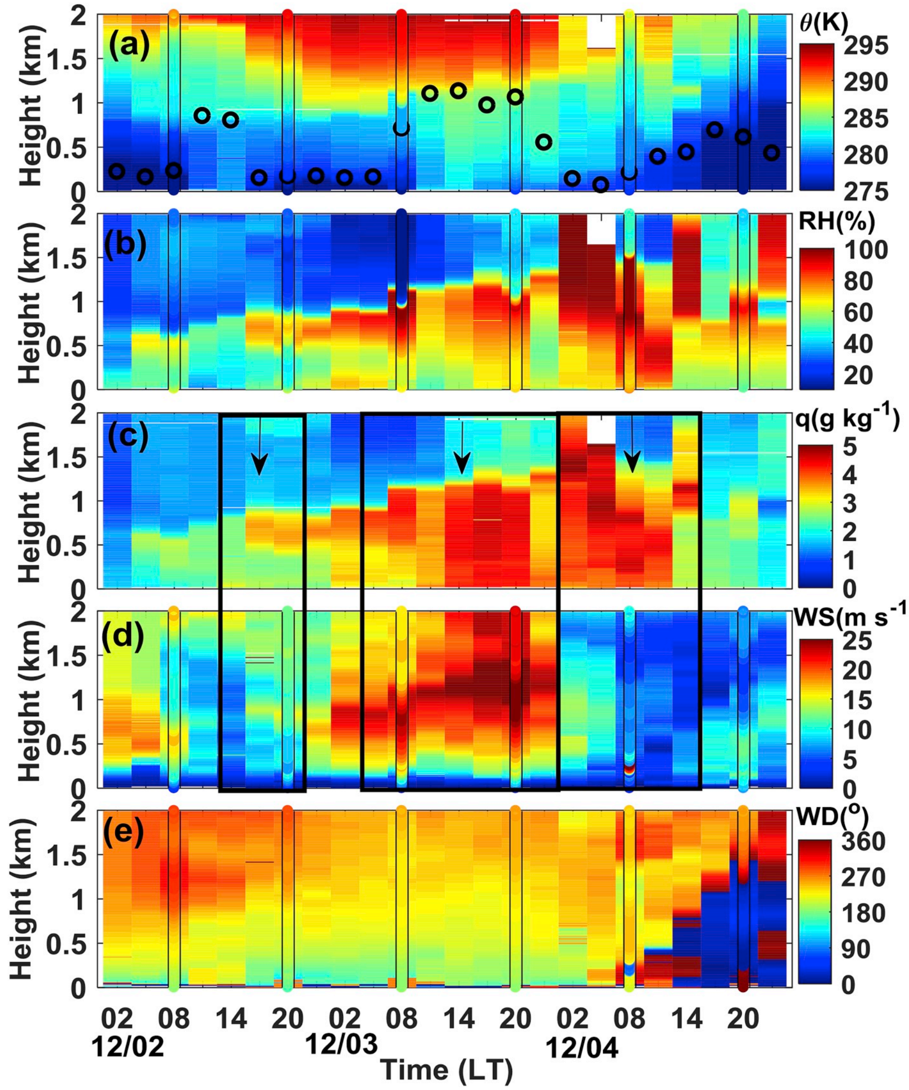

Fig. 6. Same as Fig. 5, but on December 2–4, 2016

winds, shallow boundary layer height, and high environmental humidity resulted in increase of surface PM concentration and the σ_{ext} values in the stable surface layer.

During EP2, a stronger θ inversion layer, with an average inversion intensity of about 0.02 K m^{-1} below 0.2 km, was observed to extend from the surface to 0.5 km (Figs. 6a and 7b). The strong, stable stratification profoundly suppressed vertical mixing of air pollutants, so more pollutants accumulated near the surface. This enhanced the difference between Vis_L and Vis_H during EP2 (Fig. 4b). Considering also Fig. 7b, a typical nocturnal boundary layer, with a surface stable layer decomposed from an overlying residual layer, was observed during EP2. The residual layer at 0.5–1.0 km was characterized by higher RH, q, and σ_{ext}. The exchanges of physical variables between the residual layer and the surface stable layer were quite weak.

The WS increased significantly at all altitudes during nighttime after the EP2. The maximum WS exceeded 20 m s^{-1} at altitudes below 1 km in the residual layer (Figs. 6d and 7c). Such phenomena are known as nocturnal LLJs. Rife et al. (2010) reported that the maximum WS (> 16 m s^{-1}) of the nocturnal LLJs over the Great Plains in North America usually occurred between 250 and 1000 m. Miao et al. (2018) observed that the height of the maximum LLJ WS was between 0.5 and 1.5 km in the megacities of Beijing and Guangzhou in China. The formation of EP3 was related to the nocturnal LLJs. Strong southerly LLJs began to transport large amounts of air pollutants from upstream regions to Shenyang after the 20:00 LT on December 2. These pollutants were first trapped in the residual layer, but then mixed downward after sunrise due to enhanced convective turbulence. This process reasonably explained the evolution of the vertical distribution of σ_{ext} during EP3 (Fig. 4d). In addition to air pollutants, the LLJs also carried plenty of water vapor to this region, resulting in the increase of q at all altitudes. During the EP4, WS remained lower than 5 m s^{-1} at all altitudes, which led to the re-accumulation of air pollutants near the surface. Meanwhile, high RH (70–100%) in the PBL favored to the formation of secondary aerosols. Additionally, the PBL height exhibited a distinct diurnal variation during all air pollution episodes. The top of surface stable layer at night usually less than 300 m, which favored the accumulation of pollutants near the surface. In EP3, the PBL height exceeded 1 km due to strong convective turbulence and turbulence induced by mechanical shears, which was beneficial for the vertical mixing of air pollutants in the PBL.

3.2.2. Impacts of transport and vertical mixing processes on air pollution

To clarify the transport and dispersion of air pollutants, Fig. 8 shows the spatial distribution of the simulated surface CO_2 concentrations over the Northeast China and the North China Plain before and during EP3. At 20:00 LT on December 2 (before EP3), the CO_2-rich region was distributed mainly in the eastern region of the North China Plain. The high surface CO_2 concentrations in Shenyang were mainly due to local

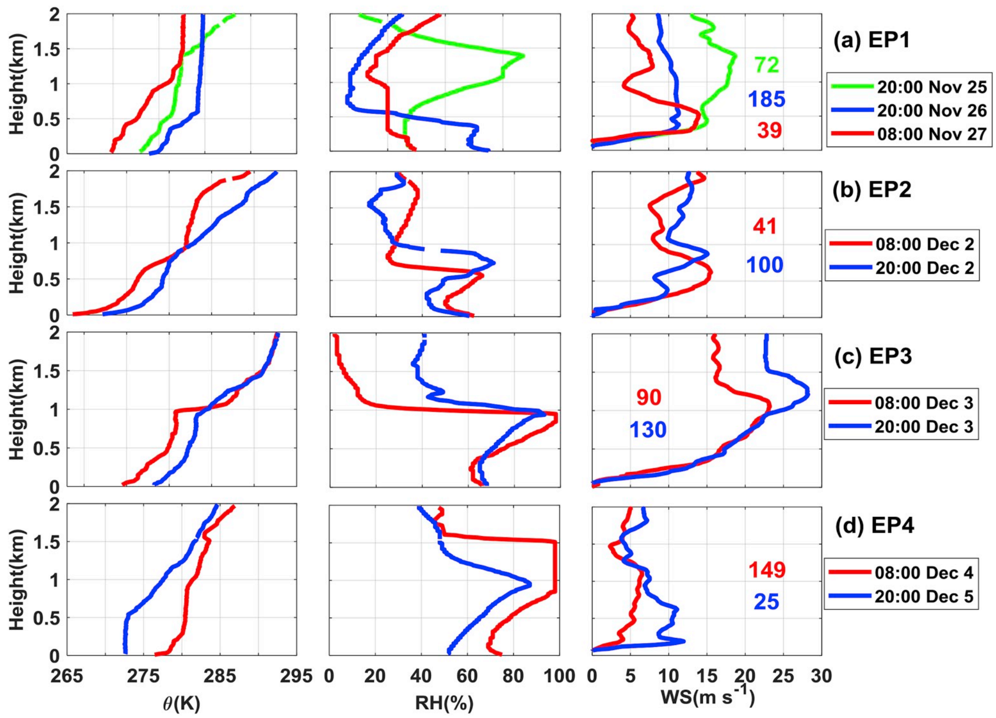

Fig. 7. Profiles of potential temperature, relative humidity, and wind speed below 2 km at 08:00 and 20:00 LT in (a) EP1, (b) EP2, (c) EP3, and (d) EP4 in Shenyang. The numbers represent the values of surface $PM_{2.5}$ concentration.

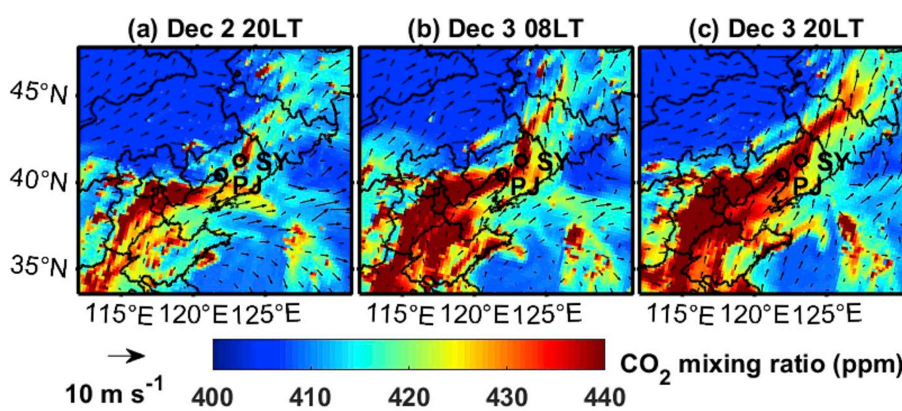

Fig. 8. Spatial distributions of surface CO_2 mixing ratio at (a) 20:00 LT on December 2, (b) 08:00 LT and (c) 20:00 LT on December 3 simulated using WRF-Chem. The location of Shenyang and Panjin is marked with black circles.

emissions, and weak winds were not favorable for the transport of air pollutants (Fig. 8a). At 08:00 LT on December 3, strong southerly and southwesterly flows transported large amounts of air pollutants from the North China Plain to Northeast China, and a CO_2 pollution belt was observed along Shenyang and Panjin (Fig. 8b). The pollution area extended farther northward due to enhanced WS at 14:00 LT on December 4 (Fig. 8c), leading to a continuous deterioration of surface air quality.

To further analyze the impacts of LLJs and convective turbulence on air pollution, Fig. 9 displays the height–latitude cross sections of CO_2 concentration (left column) and WS (right column) along the Panjin–-Shenyang line during EP3. WRF-Chem reproduced the development of LLJs during EP3. The maximum WS of the LLJs became larger and the height of the maximum WS increased from 0.5 km to 1.5 km from 02:00 LT to 14:00 LT on December 3 (Fig. 9d–f). This was consistent with the evolution of radiosonde wind profiles observed at Shenyang. Influenced by the LLJs, air pollutants were advected from south to north. After sunrise, enhanced convective turbulence resulted in a stronger vertical mixing process of air pollutants in the PBL (Fig. 9a–c).

4. Conclusions and discussion

The PBL structure plays an important role on the formation and evolution of air pollution. However, the linkage between PBL structure and air pollution in Northeast China (NEC) is not clearly understood due mainly to a lack of observations. To understand the impact of PBL structure on air pollution in this region, a PBL observational campaign was conducted from late autumn to early winter of 2016 in Shenyang, a capital city in the Northeast China. Four air pollution episodes were examined using meteorological sounding data, aerosol extinction coefficient (σ_{ext}) data retrieved from a ground-based LiDAR, and a tracer simulation with WRF-Chem. The four air pollution episodes occurred at 12:00 LT on November 26 to 07:00 LT on November 27 for EP1, 13:00–23:00 LT on December 2 for the EP2, 06:00–23:00 LT on December 3 for the EP3, and 03:00–14:00 LT on December 4 for the EP4.

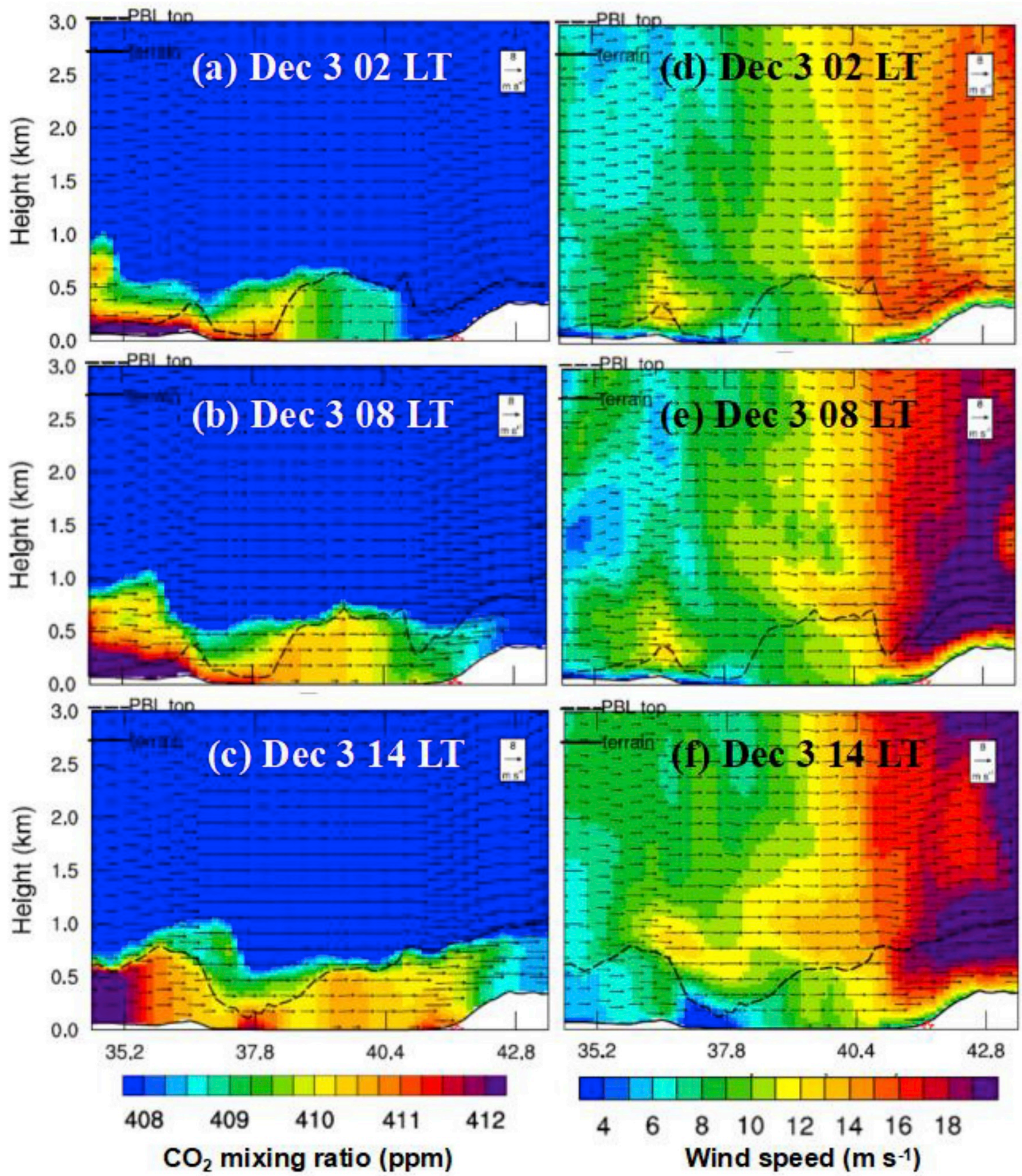

Fig. 9. Height-latitude vertical cross sections of CO_2 mixing ratio and wind speed along the Panjin-Shenyang line at (a, d) 02:00 LT, (b, e) 08:00 LT, and (c, f) 14:00 LT on December 3 simulated using WRF-Chem. The location of Shenyang is marked with a red star. (For interpretation of the references to colour in this figure legend, the reader is referred to the Web version of this article.)

Increase of $PM_{2.5}$ and PM_{10} concentrations and a decrease of visibility were observed during all air pollution episodes. In EP1, a stable and shallow surface layer (the PBL height < 400 m) formed and remained at night due to strong surface radiative cooling after a steep decline of temperature. Stable stratification and stagnant winds suppressed air pollutant dispersion, and moist air conditions in the PBL favored the secondary aerosol formation. An even stronger stable surface layer with weak winds, which was favorable to near-surface air pollutant accumulation, was observed in EP2. Enhanced local emissions during evening rush hour also contributed to the formation of EP2; high CO and NO_2 concentrations were observed during this episode. After EP2, the nocturnal LLJs developed over Shenyang. These had a maximum WS reaching 20–30 m s^{-1} at altitudes of 0.5–1.0 km. The southerly LLJs transported large amounts of air pollutants from the North China Plain to Shenyang. These pollutants were first trapped in the residual layer at nighttime and then mixed to the surface due to strong convective turbulence that developed after sunrise. The trace simulation further demonstrated the transport and mixing processes of air pollutants during EP3, which was affected by the LLJs and the development of a convective boundary layer. As the LLJs weakened, the surface PM concentrations declined at Shenyang. However, due to an approaching weak trough, air pollutants re-accumulated during EP4, because Shenyang was located in the convergence area ahead of the trough. Meanwhile, weak WS (< 6 m s^{-1}) and high RH (> 80%) at all altitudes within the PBL enhanced the deterioration of air quality near the surface.

During EP3 and EP4, heave air pollution was also observed in other regions in China, including the North China Plain and East China. Liu et al. (2019) indicated that the radiative cooling effects of elevated aerosols under stagnant winds enhanced temperature inversions, which further resulted in increases of near-surface $PM_{2.5}$ concentrations in Beijing on December 3–4, 2016. Miao et al. (2018) also indicated that the presence of aerosols within the PBL could modulate the PBL thermal structure during pollution episodes. They examined the aerosol–PBL feedback on the near-surface $PM_{2.5}$ concentration in Shenyang during December 2–4, 2016, using WRF-Chem. Their results indicated that the presence of aerosols could warm the PBL by 0.1–0.5 K and lower the near-surface temperature by 0.1–0.6 K during the daytime, and then lower the PBL height by 10–90 m. Theoretically, the change in the PBL structure could further increase the concentration of $PM_{2.5}$ near the surface. However, the concentration perturbations induced by the aerosol–PBL feedback in Shenyang ($< 5\,\mu g\,m^{-3}$) were significantly lower than the contributions of the local emissions and external transport.

Finally, the vertical gradient of visibility reflected the vertical distribution of aerosols and greatly depended on the thermal structure of the PBL. For analysis of air pollution episodes without profile measurements of aerosols, vertical measurements of visibility can be used as a proxy to elucidate understanding the linkage between air pollution and PBL structures.

Acknowledgement

This work was supported by the National Natural Science Foundation of China (41730647, 41875157, 41605112), Key Program of Science Foundation of Liaoning Meteorological Office (201904, D201603), Basic Research Funds of Central Public Welfare Research Institutes (2018SYIAEZD4), National Key R&D Program of China (No. 2017YFC0212301, 2016YFC0203304), and Key Program of Natural Science Foundation of Liaoning Province (20170520359).

Appendix A. Supplementary data

Supplementary data to this article can be found online at https://doi.org/10.1016/j.atmosenv.2019.116850.

References

Ansmann, A., Engelmann, R., Althausen, D., Wandinger, U., Hu, M., Zhang, Y., He, Q., 2005. High aerosol load over the Pearl River Delta, China, observed with Raman lidar and Sun photometer. Geophys. Res. Lett. 32 (13). https://doi.org/10.1029/2005GL023094.

Armah, F., Yawson, D., Pappoe, A.A., 2010. A systems dynamics approach to explore traffic congestion and air pollution link in the city of Accra, Ghana. Sustainability 2 (1), 252–265. https://doi.org/10.3390/su2010252.

Athanassiadis, G.A., Rao, S.T., Ku, J.Y., Clark, R.D., 2002. Boundary layer evolution and its influence on ground-level ozone concentrations. Environ. Fluid Mech. 2 (4), 339–357. https://doi.org/10.1023/A:1020456018087.

Avnery, S., Mauzerall, D.L., Liu, J., Horowitz, L.W., 2011. Global crop yield reductions due to surface ozone exposure: 1. Year 2000 crop production losses and economic damage. Atmos. Environ. 45 (13), 2284–2296. https://doi.org/10.1016/j.atmosenv.2010.11.045.

Boering, K.A., Wofsy, S.C., Daube, B.C., Schneider, H.R., Loewenstein, M., Podolske, J.R., Conway, T.J., 1996. Stratospheric mean ages and transport rates from observations of carbon dioxide and nitrous oxide. Science 274 (5291), 1340–1343. https://doi.org/10.1126/science.274.5291.1340.

Bressi, M., Sciare, J., Ghersi, V., Bonnaire, N., Nicolas, J.B., Petit, J.E., Moukhtar, S., Rosso, A., Mihalopoulos, N., Féron, A., 2013. A one-year comprehensive chemical characterisation of fine aerosol ($PM_{2.5}$) at urban, suburban and rural background sites in the region of Paris (France). Atmos. Chem. Phys. 13 (15), 7825–7844. https://doi.org/10.5194/acp-13-7825-2013.

Che, H., Qi, B., Zhao, H., Xia, X., Eck, T.F., Goloub, P., Dubovik, O., Estelles, V., Cuevas-Agulló, E., Blarel, L., Wu, Y., Zhu, J., Du, R., Wang, Y., Wang, H., Gui, K., Yu, J., Zheng, Y., Sun, T., Chen, Q., Shi, G., Zhang, X., 2018. Aerosol optical properties and direct radiative forcing based on measurements from the China Aerosol Remote Sensing Network (CARSNET) in eastern China. Atmos. Chem. Phys. 18, 405–425. https://doi.org/10.5194/acp-18-405-2018.

Chen, F., Dudhia, J., 2001. Coupling an advanced land surface-hydrology model with the Penn State-NCAR MM5 modeling system. Part I: model implementation and sensitivity. Mon. Weather Rev. 129 (4), 569–585. https://doi.org/10.1175/1520-0493(2001)129<0569:Caalsh>2.0.Co;2.

Chen, Z.H., Cheng, S.Y., Li, J.B., Guo, X.R., Wang, W.H., Chen, D.S., 2008. Relationship between atmospheric pollution processes and synoptic pressure patterns in northern China. Atmos. Environ. 42 (24), 6078–6087. https://doi.org/10.1016/j.atmosenv.2008.03.043.

Chen, J., Zhao, C.S., Ma, N., Liu, P.F., Göbel, T., Hallbauer, E., Deng, Z.Z., Ran, L., Xu, W.Y., Liu, H.J., Yan, P., Zhou, X.J., Wiedensohler, A., 2012. A parameterization of low visibilities for hazy days in the North China Plain. Atmos. Chem. Phys. 12 (11), 4935–4950. https://doi.org/10.5194/acp-12-4935-2012.

Chen, R., Peng, R.D., Meng, X., Zhou, Z., Chen, B., Kan, H., 2013. Seasonal variation in the acute effect of particulate air pollution on mortality in the China Air Pollution and Health Effects Study (CAPES). Sci. Total Environ. 450, 259–265. https://doi.org/10.1016/j.scitotenv.2013.02.040.

Cheng, Z., Wang, S., Fu, X., Watson, J.G., Jiang, J., Fu, Q., Chen, C., Xu, B., Yu, J., Chow, J.C., Hao, J., 2014. Impact of biomass burning on haze pollution in the Yangtze River delta, China: a case study in summer 2011. Atmos. Chem. Phys. 14 (9), 4573–4585. https://doi.org/10.5194/acp-14-4573-2014.

Ding, A.J., Fu, C.B., Yang, X.Q., Sun, J.N., Petäjä, T., Kerminen, V.M., Wang, T., Xie, Y., Herrmann, E., Zheng, L.F., Nie, W., 2013. Intense atmospheric pollution modifies weather: a case of mixed biomass burning with fossil fuel combustion pollution in eastern China. Atmos. Chem. Phys. 13 (20), 10545–10554. https://doi.org/10.5194/acp-13-10545-2013.

Dudhia, J., 1989. Numerical study of convection observed during the winter monsoon experiment using a mesoscale two-dimensional model. J. Atmos. Sci. 46 (20), 3077–3107. https://doi.org/10.1175/1520-0469(1989)046<3077:Nsocod>2.0.Co;2.

Gao, S., Wang, Y., Huang, Y., Zhou, Q., Lu, Z., Shi, X., Liu, Y., 2016. Spatial statistics of atmospheric particulate matter in China. Atmos. Environ. 134, 162–167. https://doi.org/10.1016/j.atmosenv.2016.03.052.

Guo, S., Hu, M., Zamora, M.L., Peng, J., Shang, D., Zheng, J., Du, Z., Wu, Z., Shao, M., Zeng, L., Molina, M.J., 2014. Elucidating severe urban haze formation in China. Proc. Natl. Acad. Sci. 111 (49), 17373–17378. https://doi.org/10.1073/pnas.1419604111.

Guo, J., Miao, Y., Zhang, Y., Liu, H., Li, Z., Zhang, W., He, J., Lou, M., Yan, Y., Bian, L., Zhai, P., 2016. The climatology of planetary boundary layer height in China derived from radiosonde and reanalysis data. Atmos. Chem. Phys. 16 (20), 13309–13319. https://doi.org/10.5194/acp-16-13309-2016.

Han, S., Liu, J., Hao, T., Zhang, Y., Li, P., Yang, J., Wang, Q., Cai, Z., Yao, Q., Zhang, M., Wang, X., 2018. Boundary layer structure and scavenging effect during a typical winter haze-fog episode in a core city of BTH region, China. Atmos. Environ. 179, 187–200. https://doi.org/10.1016/j.atmosenv.2018.02.023.

Hintsa, E.J., Boering, K.A., Weinstock, E.M., Anderson, J.G., Gary, B.L., Pfister, L., Daube, B.C., Wofsy, S.C., Loewenstein, M., Podolske, J.R., Margitan, J.J., 1998. Troposphere-to-stratosphere transport in the lowermost stratosphere from measurements of H_2O, CO_2, N_2O and O_3. Geophys. Res. Lett. 25 (14), 2655–2658. https://doi.org/10.1029/98GL01797.

Hong, S.Y., 2010. A new stable boundary-layer mixing scheme and its impact on the simulated East Asian summer monsoon. Q. J. Roy. Meteor. Soc. 136, 1481–1496. https://doi.org/10.1002/qj.665.

Hong, S.Y., Noh, Y., Dudhia, J., 2006. A new vertical diffusion package with an explicittreatment of entrainment processes. Mon. Weather Rev. 134 (9), 2318–2341. https://doi.org/10.1175/Mwr3199.1.

Hu, X.-M., Doughty, D.C., Sanchez, K.J., Joseph, E., Fuentes, J.D., 2012. Ozone variability in the atmospheric boundary layer in Maryland and its implications for vertical transport model. Atmos. Environ. 46, 354–364. https://doi.org/10.1016/j.atmosenv.2011.09.054.

Hu, X.-M., Klein, P.M., Xue, M., Zhang, F., Doughty, D.C., Forkel, R., Joseph, E., Fuentes, J.D., 2013a. Impact of the vertical mixing induced by low-level jets on boundary layer ozone concentration. Atmos. Environ. 70, 123–130. https://doi.org/10.1016/j.atmosenv.2012.12.046.

Hu, X.-M., Klein, P.M., Xue, M., Lundquist, J.K., Zhang, F., Qi, Y., 2013b. Impact of low-level jets on the nocturnal urban heat island intensity in Oklahoma City. J. Appl. Meteorol. Climatol. 52 (8), 1779–1802. https://doi.org/10.1175/JAMC-D-12-0256.1.

Hu, X.-M., Ma, Z., Lin, W., Zhang, H., Hu, J., Wang, Y., Xu, X., Fuentes, J.D., Xue, M., 2014. Impact of the Loess Plateau on the atmospheric boundary layer structure and air quality in the North China Plain: a case study. Sci. Total Environ. 499, 228–237. https://doi.org/10.1016/j.scitotenv.2014.08.053.

Hu, X.-M., Li, X., Xue, M., Wu, D., Fuentes, J.D., 2016. the formation of barrier winds East of the loess plateau and their effects on dispersion conditions in the North China plains. Boundary-Layer Meteorol. 161 (1), 1–19. https://doi.org/10.1007/s10546-016-0159-4.

Hu, J., Li, Y., Zhao, T., Liu, J., Hu, X.M., Liu, D., Jiang, Y., Xu, J., Chang, L., 2018. An important mechanism of regional O_3 transport for summer smog over the Yangtze River Delta in eastern China. Atmos. Chem. Phys. 18 (22), 16239–16251. https://doi.org/10.5194/acp-18-16239-2018.

Hu, X.-M., Crowell, S., Wang, Q., Zhang, Y., Davis, K.J., Xue, M., Xiao, X., Moore, B., Wu, X., Choi, Y., DiGangi, J.,P., 2019. CO_2 Dynamical Downscaling in 2016 over the contiguous United States using WRF-VPRM, a weather-biosphere-online-coupled model. J. Geophys. Res (under revision).

Kampa, M., Castanas, E., 2008. Human health effects of air pollution. Environ. Pollut. 151 (2), 362–367. https://doi.org/10.1016/j.envpol.2007.06.012.

Kan, H., Chen, R., Tong, S., 2012. Ambient air pollution, climate change, and population health in China. Environ. Int. 42, 10–19. https://doi.org/10.1016/j.envint.2011.03.003.

Kanamitsu, M., Ebisuzaki, W., Woollen, J., Yang, S.-K., Hnilo, J.J., Fiorino, M., Potter, G.L., 2002. NCEP–DOE AMIP-II reanalysis (R-2). Bull. Am. Meteorol. Soc. 83 (11), 1631–1644. https://doi.org/10.1175/BAMS-83-11-1631.

Klein, P.M., Hu, X.-M., Xue, M., 2014. Impacts of mixing processes in nocturnal atmospheric boundary layer on urban ozone concentrations. Boundary-Layer Meteorol. 150 (1), 107–130. https://doi.org/10.1007/s10546-013-9864-4.

Li, Y., Deng, J., Mu, C., Xing, Z., Du, K., 2014. Vertical distribution of CO_2 in the atmospheric boundary layer: characteristics and impact of meteorological variables. Atmos. Environ. 91, 110–117. https://doi.org/10.1016/j.atmosenv.2014.03.067.

Li, X., Ma, Y., Wang, Y., Liu, N., Hong, Y., 2017. Temporal and spatial analyses of particulate matter (PM10 and PM2.5) and its relationship with meteorological parameters over an urban city in northeast China. Atmos. Res. 198, 185–193. https://doi.org/10.1016/j.atmosres.2017.08.023.

Li, X., Wang, Y., Shen, L., Zhang, H., Zhao, H., Zhang, Y., Ma, Y., 2018a. Characteristics of boundary layer structure during a persistent haze event in the Central Liaoning City Cluster, Northeast China. J. Meteorol. Res. 32 (2), 302–312. https://doi.org/10.1007/s13351-018-7053-6.

Li, X., Wang, Y., Zhao, H., Hong, Y., Liu, N., Ma, Y., 2018b. Characteristics of pollutants and boundary layer structure during two haze events in summer and autumn 2014 in Shenyang, Northeast China. Aerosol Air Qual. Res. 18 (2), 386–396. https://doi.org/10.4209/aaqr.2017.03.0100.

Lin, J.C., Mitchell, L., Crosman, E., Mendoza, D.L., Buchert, M., Bares, R., Fasoli, B., Bowling, D.R., Pataki, D., Catharine, D., Strong, C., 2018. CO_2 and carbon emissions from cities: linkages to air quality, socioeconomic activity, and stakeholders in the salt lake city urban area. Bull. Am. Meteorol. Soc. 99 (11), 2325–2339. https://doi.org/10.1175/BAMS-D-17-0037.1.

Liu, S., Liu, Z., Li, J., Wang, Y., Ma, Y., Sheng, L., Liu, H., Liang, F., Xin, G., Wang, J., 2009. Numerical simulation for the coupling effect of local atmospheric circulations over the area of Beijing, Tianjin and Hebei province. Sci. China Ser. D Earth Sci. 52 (3), 382–392. https://doi.org/10.1007/s11430-009-0030-2.

Liu, J., Fan, S., Wu, D., Wu, M., Liao, Z.H., Li, H.W., 2015. Boundary layer characteristics of typical haze process in the Pearl River Delta region. China Environ. Sci. 35 (6), 1664–1674 (in Chinese).

Liu, L., Zhang, X., Zhong, J., Wang, J., Yang, Y., 2019. The 'two-way feedback mechanism' between unfavorable meteorological conditions and cumulative $PM_{2.5}$ mass existing in polluted areas south of Beijing. Atmos. Environ. 208, 1–9. https://doi.org/10.1016/j.atmosenv.2019.02.050.

Ma, Y., Zhao, H., Dong, Y., Che, H., Li, X., Hong, Y., Li, X., Yang, H., Liu, Y., Wang, Y., Liu, N., Sun, C., 2018. Comparison of two air pollution episodes over Northeast China in winter 2016/17 using ground-based lidar. J. Meteorol. Res. 32 (2), 313–323. https://doi.org/10.1007/s13351-018-7047-4.

Miao, Y., Liu, S., 2019. Linkages between aerosol pollution and planetary boundary layer structure in China. Sci. Total Environ. 650, 288–296. https://doi.org/10.1016/j.scitotenv.2018.09.032.

Miao, Y., Guo, J., Liu, S., Liu, H., Li, Z., Zhang, W., Zhai, P., 2017. Classification of summertime synoptic patterns in Beijing and their associations with boundary layer structure affecting aerosol pollution. Atmos. Chem. Phys. 17 (4), 3097–3110. https://doi.org/10.5194/acp-17-3097-2017.

Miao, Y., Guo, J., Liu, S., Zhao, C., Li, X., Zhang, G., Wei, W., Ma, Y., 2018. Impacts of synoptic condition and planetary boundary layer structure on the trans-boundary aerosol transport from Beijing-Tianjin-Hebei region to northeast China. Atmos. Environ. 181, 1–11. https://doi.org/10.1016/j.atmosenv.2018.03.005.

Mlawer, E.J., Taubman, S.J., Brown, P.D., Iacono, M.J., Clough, S.A., 1997. Radiative transfer for inhomogeneous atmospheres: RRTM, a validated correlated-k model for the longwave. J. Geophys. Res. 102 (D14), 16663–16682. https://doi.org/10.1029/97jd00237.

Morrison, H., Thompson, G., Tatarskii, V., 2009. Impact of cloud microphysics on the Development of trailing stratiform precipitation in a simulated squall line: comparison of one- and two-moment schemes. Mon. Weather Rev. 137 (3), 991–1007. https://doi.org/10.1175/2008mwr2556.1.

Nielsen-Gammon, J.W., Powell, C.L., Mahoney, M.J., Angevine, W.M., Senff, C., White, A., 2008. Multisensor estimation of mixing heights over a coastal city. J. Appl. Meteorol. Climatol. 47, 27–43. https://doi.org/10.1175/2007JAMC1503.1.

Oda, T., Maksyutov, S., Andres, R.J., 2018. The Open-source Data Inventory for Anthropogenic CO_2, version 2016 (ODIAC2016): a global monthly fossil fuel CO_2 gridded emissions data product for tracer transport simulations and surface flux inversions. Earth Syst. Sci. Data 10 (1), 87–107. https://doi.org/10.5194/essd-10-87-2018.

Peters, W., Jacobson, A.R., Sweeney, C., Andrews, A.E., Conway, T.J., Masarie, K., Miller, J.B., Bruhwiler, L.M., Pétron, G., Hirsch, A.I., Worthy, D.E.J., van der Werf, G.R., Randerson, J.T., Wennberg, P.O., Krol, M.C., Tans, P.P., 2007. An atmospheric perspective on North American carbon dioxide exchange: CarbonTracker. Proc. Natl. Acad. Sci. 104 (48), 18925–18930. https://doi.org/10.1073/pnas.0708986104.

Ren, Y., Zhang, H., Wei, W., Wu, B., Cai, X., Song, Y., 2019. Effects of turbulence structure and urbanization on the heavy haze pollution process. Atmos. Chem. Phys. 19 (2), 1041–1057. https://doi.org/10.5194/acp-19-1041-2019.

Richardson, E.A., Pearce, J., Tunstall, H., Mitchell, R., Shortt, N.K., 2013. Particulate air pollution and health inequalities: a Europe-wide ecological analysis. Int. J. Health Geogr. 12 (1), 1–10. 34. https://doi.org/10.1186/1476-072X-12-34.

Rife, D.L., Pinto, J.O., Monaghan, A.J., Davis, C.A., Hannan, J.R., 2010. Global distribution and characteristics of diurnally varying low-level jets. J. Clim. 23 (19), 5041–5064. https://doi.org/10.1175/2010JCLI3514.1.

Seidel, D.J., Zhang, Y., Beljaars, A., Golaz, J.-C., Jacobson, A.R., Medeiros, B., 2012. Climatology of the planetary boundary layer over the continental United States and Europe. J. Geophys. Res. Atmos. 117, 1–15. https://doi.org/10.1029/2012JD018143.

Seinfeld, J.H., Pandis, S.N., 2016. Atmospheric Chemistry and Physics: from Air Pollution to Climate Change, third ed. John Wiley & Sons.

Stull, R.B., 1988. An Introduction to Boundary Layer Meteorology, vol. 8. Atmospheric Sciences Library, pp. 499–543.

Tang, G., Zhang, J., Zhu, X., Song, T., Münkel, C., Hu, B., Schäfer, K., Liu, Z., Zhang, J., Wang, L., Xin, J., Suppan, P., Wang, Y., 2016. Mixing layer height and its implications for air pollution over Beijing, China. Atmos. Chem. Phys. 16, 2459–2475. https://doi.org/10.5194/acp-16-2459-2016.

Tao, R., Che, H.Z., Chen, Q.L., Tao, J., Wang, Y.Q., Sun, J.Y., Wang, H., Zhang, X.Y., 2014. Study of aerosol optical properties based on ground measurements over Sichuan Basin, China. Aerosol Air Qual. Res. 14 (3), 905–915. https://doi.org/10.4209/aaqr.2013.04.0125.

Wang, J.L., Kotamarthi, V.R., 2014. Downscaling with a nested regional climate model in near-surface fields over the contiguous United States. J. Geophys. Res. 119 (14), 8778–8797. https://doi.org/10.1002/2014jd021696.

Wang, Y., Yao, L., Wang, L., Liu, Z., Ji, D., Tang, G., Zhang, J., Sun, Y., Hu, B., Xin, J., 2014. Mechanism for the formation of the January 2013 heavy haze pollution episode over central and eastern China. Sci. China Earth Sci. 57 (1), 14–25. https://doi.org/10.1007/s11430-013-4773-4.

Wang, M., Cao, C., Li, G., Singh, R.P., 2015. Analysis of a severe prolonged regional haze episode in the Yangtze River Delta, China. Atmos. Environ. 102, 112–121. https://doi.org/10.1016/j.atmosenv.2014.11.038.

Wang, H., Shi, G., Tian, M., Zhang, L., Chen, Y., Yang, F., Cao, X., 2017. Aerosol optical properties and chemical composition apportionment in Sichuan Basin, China. Sci. Total Environ. 577, 245–257. https://doi.org/10.1016/j.scitotenv.2016.10.173.

Wei, W., Zhang, H., Wu, B., Huang, Y., Cai, X., Song, Y., Li, J., 2018. Intermittent turbulence contributes to vertical dispersion of $PM_{2.5}$ in the North China Plain: cases from Tianjin. Atmos. Chem. Phys. 18 (17), 12953–12967. https://doi.org/10.5194/acp-18-12953-2018.

Wu, D., Bi, X., Deng, X., Li, F., Tan, H., Liao, G., Huang, J., 2007. Effect of atmospheric haze on the deterioration of visibility over the Pearl River Delta. J. Meteorol. Res. 21 (2), 215–223.

Yang, Y., Hu, X.-M., Gao, S., Wang, Y., 2019. Sensitivity of WRF simulations with the YSU PBL scheme to the lowest model level height for a sea fog event over the Yellow Sea. Atmos. Res. 215, 253–267. https://doi.org/10.1016/j.atmosres.2018.09.004.

Ye, X., Song, Y., Cai, X., Zhang, H., 2016. Study on the synoptic flow patterns and boundary layer process of the severe haze events over the North China Plain in January 2013. Atmos. Environ. 124, 129–145. https://doi.org/10.1016/j.atmosenv.2015.06.011.

Zhang, G., Bi, X., Chan, L.Y., Wang, X., Sheng, G., Fu, J., 2013. Size-segregated chemical characteristics of aerosol during haze in an urban area of the Pearl River Delta region, China. Urban Clim. 4, 74–84. https://doi.org/10.1016/j.uclim.2013.05.002.

Zhang, R.H., Li, Q., Zhang, R.N., 2014. Meteorological conditions for the persistent severe fog and haze event over eastern China in January 2013. Sci. China Earth Sci. 57 (1), 26–35. https://doi.org/10.1007/s11430-013-4774-3.

Zhao, C., Wang, Y., Zeng, T., 2009. East China plains: a "basin" of ozone pollution. Environ. Sci. Technol. 43 (6), 1911–1915. https://doi.org/10.1021/es8027764.

Zhao, X.J., Zhao, P.S., Xu, J., Meng, W., Pu, W.W., Dong, F., He, D., Shi, Q.F., 2013. Analysis of a winter regional haze event and its formation mechanism in the North China Plain. Atmos. Chem. Phys. 13 (11), 5685–5696. https://doi.org/10.5194/acp-13-5685-2013.

Zhao, H., Che, H., Xia, X., Wang, Y., Wang, H., Wang, P., Ma, Y., Yang, H., Liu, Y., Wang, Y., Gui, K., Sun, T., Zheng, Y., Zhang, X., 2018a. Multi-year ground-based measurements of aerosol optical properties and direct radiative effect over different surface types in northeastern China. J. Geophys. Res.: Atmosphere 123 (24), 13887–13916. https://doi.org/10.1029/2018JD029141.

Zhao, H., Che, H., Wang, Y., Dong, Y., Ma, Y., Li, X., Hong, Y., Yang, H., Liu, Y., Wang, Y., Gui, K., Sun, T., Zheng, Y., Zhang, X., 2018b. Aerosol vertical distribution and typical air pollution episodes over Northeastern China during 2016 analyzed by ground-based Lidar. Aerosol Air Qual. Res. 18 (4), 918–937. https://doi.org/10.4209/aaqr.2017.09.0327.

Zhong, J., Zhang, X., Dong, Y., Wang, Y., Liu, C., Wang, J., Zhang, Y., Che, H., 2018. Feedback effects of boundary-layer meteorological factors on cumulative explosive growth of $PM_{2.5}$ during winter heavy pollution episodes in Beijing from 2013 to 2016. Atmos. Chem. Phys. 18 (1), 247–258. https://doi.org/10.5194/acp-18-247-2018.

Zhu, J., Liao, H., Li, J., 2012. Increases in aerosol concentrations over eastern China due to the decadal-scale weakening of the East Asian summer monsoon. Geophys. Res. Lett. 39 (9), L09809. https://doi.org/10.1029/2012GL051428.